ROYAL SOCIETY OF CHEMISTRY

PAPER

Check for updates

Tautomer identification troubles: the molecular structure of itaconic and citraconic anhydride revealed by rotational spectroscopy†

Alexander Kanzow, [ID] [a] Beppo Hartwig, [ID] [a] Philipp Buschmann, [b]
Kevin G. Lengsfeld, [b] Cara M. Höhne, [b] Joshua S. Hoke, ‡ [a] Finn Knüppe, ‡ [a]
Finn Köster, ‡ [a] Jakob K. van Spronsen, ‡ [a] Jens-Uwe Grabow, [ID] [b]
Don McNaughton [ID] [c] and Daniel A. Obenchain [ID] * [a]

Microwave spectra of citraconic anhydride and its tautomer itaconic anhydride have been recorded in a frequency range of 6–18 GHz. Both a- and b-type transitions were observed for both tautomers, while c-type transitions could only be observed for the E torsional symmetry state of citraconic anhydride. For both molecules, a molecular substitution structure, r_S, was obtained by measurements of mono-substituted ^{13}C isotopologues in natural abundance. For citraconic anhydride, ^{18}O isotopologues were also observed and the V_3 barrier to internal rotation has been determined at 326.5153(61) cm^{-1}. In addition to the microwave spectra, a gas-phase study of isomerisation between the tautomers was carried out, which was assisted by theoretical transition state calculations, employing a variety of different density functionals as well as the wavefunction based Møller–Plesset perturbation theory, MP2, and coupled cluster methods, CCSD(T)-F12c and DCSD-F12b. These were also used to benchmark the experimentally determined r_S structures and V_3 barrier of rotation in citraconic anhydride. *Via* theoretical ground state vibrational calculations, semi-experimental equilibrium structure, $r_{0 \rightarrow e}^{SE}$, were derived for each theoretical method and were compared to the coupled cluster equilibrium structures, r_e. In addition, mass dependent $r_m^{(1)}$ and $r_m^{(2)}$ fits were conducted to obtain approximate r_e structures. Using the determined structures we can revise a previous study that misidentified citraconic anhydride as itaconic anhydride.

1 Introduction

Citraconic anhydride (CA) and its tautomer, itaconic anhydride (IA) are unsaturated cyclic acid anhydrides which are employed as simple building blocks in a variety of organic syntheses, including Diels–Alder reactions[1] and Friedel–Crafts-acylations.[2] They are also employed in radical copolymerizations to modify

[a] *Institute für Physikalische Chemie, Georg-August-Universität Göttingen, Tammannstraße 6, 37077 Göttingen, Germany. E-mail: daniel.obenchain@uni-goettingen.de*
[b] *Institut für Physikalische Chemie und Elektrochemie, Gottfried Wilhelm Leibniz Universität, Callinstraße 3A, 30167 Hannover, Germany*
[c] *School of Chemistry, Monash University, Wellington Road, 3800 Clayton, Australia*

† Electronic supplementary information (ESI) available: We provide figures of the molecules in the inertial principal axis system, the experimental and predicted rotational fitting parameters, results of the structure determination and example inputs for the computations. In addition, the raw microwave spectra (https://doi.org/10.25625/FQCEVB), all computational outputs (https://doi.org/10.25625/IBKABW) as well as the outputs of the experimental and structure fits (https://doi.org/10.25625/AFCLSC) are provided.
‡ These authors contributed equally to this work.

the solubility of a polymer in different solvents.[3] The electrophilic anhydride functional group of these polymers is also used to interact with nucleophilic *N*-sites of amino acids and proteins which leads to a reversible blocking of the proteinogenic function.[4,5] In the past, the structurally related maleic anhydride (MA) has been extensively studied. An advantage that CA and IA have over MA is the fact that they are available from renewable resources. It has been known for a long time, that itaconic acid can be obtained from the fermentation of glucose with certain fungi, most notably *Aspergillus terreus*.[6] From itaconic acid, through dehydration, both CA and IA can be obtained,[7,8] which makes them attractive for sustainable chemistry.

However, despite all these interesting and promising properties, very little thermodynamical and structural data is available for these compounds, as only IA has been reported to be studied by microwave spectroscopy before.[9] In conjunction with collecting data for these interesting compounds, prospects of isomerization between the two isomers are also of great interest, helping to improve the fundamental understanding of chemical reactions and thermodynamic equilibria. Understanding of gas-phase

This journal is © the Owner Societies 2025

Phys. Chem. Chem. Phys., 2025, **27**, 9491–9503 | **9491**

isomerization is also important in industrial fuel production, as it is the pathway through which higher octane numbers are produced from less branched alkanes.[10]

Despite CA and IA being tautomers of each other, the structure and relative thermodynamic stability significantly differ, as CA forms a conjugated 6π system and may be labeled as pseudo-aromatic compound, whereas IA only forms a conjugated 4π system, which suggests that CA is the more stable isomer.

In this study, both compounds were characterised separately using microwave spectroscopy and the differing moments of inertia allow us to distinguish between CA and IA. Microwave spectroscopy is especially well suited for these molecules as they possess large dipole moments and moderate vapor pressure, allowing for the observation of many high J transitions.

The previous microwave study that reports the structure of IA finds that there is a large-amplitude motion in the ground vibrational state that leads to a doubling of the rotational transitions. We show in this work that the observed doubling is from a methyl-top internal rotation of CA. Likely, the IA sample used by McMahon et al.[9] isomerized, and with CA having a large vapor pressure, was mistakenly identified as the IA. A recent K_a-band study of succinimide and N-chloro-succinimide did not report any doubling due to a large-amplitude motion.[11]

With the ability to conduct high-precision measurements in the cold isolated gas phase of these compounds, our investigation lends itself to a benchmarking study since these conditions are ideal for quantum chemical methods, which supplement our results.

2 Methods

2.1 Fourier transform chirp-excitation rotational spectroscopy

An initial broadband measurement was completed on the IMPACT (in-phase/quadrature-phase-modulation passage-acquired-coherence technique) spectrometer in Hannover[12] from 12.5 GHz–15.5 GHz. The sample of citraconic anhydride (98%) was purchased from Sigma-Aldrich and heated in the nozzle reservoir to a temperature of 373 K (100 °C). Argon gas was then used as a carrier gas at 0.2 MPa (2.0 bar) absolute pressure. The spectrum showed transitions based on the rotational constants given by McMahon et al. for itaconic anhydride and a new set of transitions. To understand this previous assignment and the observations on the IMPACT spectrometer, we began additional measurements using a cavity FTMW instrument.

2.2 Fourier-transform microwave cavity spectroscopy

Commercial samples of citraconic anhydride (98%) and itaconic anhydride (95%) obtained from Sigma-Aldrich were used without further purification. The spectra were taken on a pulsed-jet Fabry–Perot-type resonator in Göttingen, Q-CUMBER (Q-factor cavity utilising molecular beam electric resonator), in the range of 6–18 GHz. The exact experimental setup is similar to the one previously described in ref. 13. The rotational transitions were measured using the FTMW++ program[14] in a narrow spectral width of about 2 MHz, allowing for high-precision measurements. While citraconic anhydride samples were heated to temperatures of around 333 K (60 °C), itaconic anhydride was heated to temperatures between 343 K (70 °C) and 373 K (100 °C). Ne was used as the carrier gas for both compounds with an absolute pressure of 0.10 MPa (1.0 bar). The free induction decay (FID) was recorded for at least 51.2 μs up to 819.2 μs and varies for each transition. This variation was to reduce the required number of averages when higher resolution was not required for overlapping transitions. Not all transitions could be fully resolved. Depending on the intensity of the transition, up to 11 000 FIDs were averaged to achieve the minimum signal-to-noise ratio of at least 3 : 1.

2.3 Computational methods

Theoretical geometry optimizations were performed using the Gaussian 16 suite (Rev. C.01)[15] and Molpro 2022.3.[16–18] First, we describe the calculations conducted with the Gaussian program package in detail. Several density functional theory (DFT) methods were utilized alongside Møller–Plesset perturbation theory of second order (MP2),[19–24] to obtain a comparison with a wavefunction based post Hartree–Fock (HF) method. The employed DFT methods cover a large span of the computational cost scale. The least expensive functionals used were the hybrid functionals PBE0[25,26] and B3LYP[27–30] which use a constant amount of exact HF exchange. CAM-B3LYP,[31] as the next more expensive method, improves on B3LYP by adding long range Coulomb-correction.[32] This is also employed in LC-ωPBE[33,34] which can be seen as the PBE0 equivalent of CAM-B3LYP. Next up is M06-2X,[35] which is a meta-hybrid functional of the Truhlar group. The span is topped by two double-hybrid functionals, B2PLYP and DSD-PBEP86,[36,37] the former being the original double-hybrid functional proposed by S. Grimme.[38,39] Both methods incorporate parts of the correlation energy from the wavefunction based MP2, which itself comes at a similar cost to the double hybrid functionals. DSD-PBEP86 utilises so-called spin component scaled MP2 (SCS-MP2), initially proposed by S. Grimme,[40] which should yield improved results over traditional MP2 methods coupled with DFT like B2PLYP.

For all methods mentioned above, an augmented version of Dunning's correlation consistent basis set at the triple-ζ level (aug-cc-pVTZ)[41,42] was utilised as the basis set of choice and Grimme's D3 dispersion correction was added in conjunction with Becke–Johnson damping (D3(BJ))[43,44] when possible. No additional dispersion correction was applied when using M06-2X or MP2. The M06-2X functional, by design, is supposed to correctly describe dispersion interactions. The SuperFine integration grid and VeryTight optimization criteria were used for all geometry optimizations with the different previously mentioned methods. In case of MP2, no integration grid is necessary. Following the geometry optimizations, an anharmonic vibrational frequency calculation was conducted using vibrational perturbation theory of second order (VPT2)[45–47] to account for zero-point contributions to the rotational constants and to obtain quartic centrifugal distortion constants.

9492 | *Phys. Chem. Chem. Phys.*, 2025, **27**, 9491–9503

This journal is © the Owner Societies 2025

To go beyond the MP2 method on the wavefunction theory side we used the Molpro program package (version 2022.3)[16–18] to conduct "gold standard" CCSD(T) calculations. CCSD(T) refers to coupled cluster[48,49] with an iterative treatment of single and double excitations (singles and doubles), while using a non-iterative perturbative approximation for the triples calculation. The optimized geometries at the CCSD(T) level can then be used as references for our semi-experimental equilibrium structures. Custom convergence criteria were used for the optimizations yielding tightly converged structures. Additionally, harmonic frequency calculations have been conducted to verify the presence of a minimum. To accelerate the basis set convergence the explicitly correlated CCSD(T)-F12c[50–54] method is used. Such explicitly correlated methods are currently not available in Gaussian. Additionally, a variant of CCSD as implemented in Molpro is used, utilizing the so called distinguishable cluster approximation (DCSD[50,55,56]), which has been shown to greatly increase CCSD's accuracy while keeping its computational scaling. Explicit correlation is also employed in this case (DCSD-F12b[57]). We used the orbital basis set cc-pVDZ-F12[58] as well as the cc-pVDZ-F12/OPTRI[59] and cc-pVDZ-F12/MP2FIT[60] basis sets used for density fitting. These basis sets were specifically designed to be used with explicitly correlated methods.

For the scan of the methyl top potential energy surface (PES), the SuperFine integration grid and tight geometry optimization criteria were used for 1° steps of the methyl top torsional angle α in the interval between 0° and 60°. These calculations were conducted with Gaussian for all previously mentioned methods. The torsional angle α is defined as the dihedral angle $\angle(C_5, C_4, C_9, H_{10})$, according to the numbering scheme shown in Fig. 1 and thus shows an energetic minimum at $\alpha(n) = 2n\pi/3$, $n \in \mathbb{Z}$.

An overview of all methods used and example inputs can be found in Section S4 of the ESI.†

3 Results

Both constitutional isomers, citraconic anhydride (CA) and itaconic anhydride (IA) were thoroughly characterized using
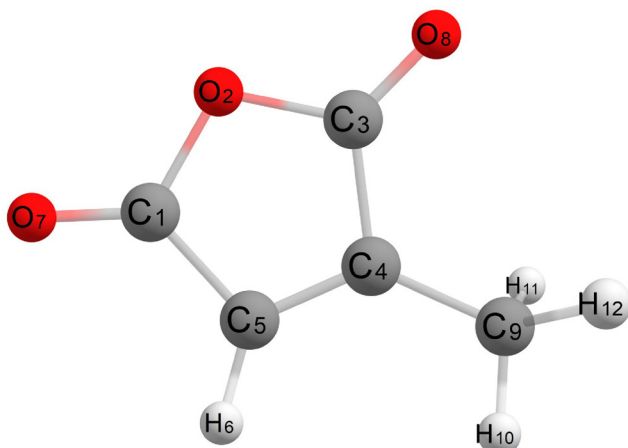
FTMW pulse-excitation narrowband spectroscopy. Chirp-excitation broadband data alongside *ab initio* predictions were used for initial fitting of the rotational constants and then followed up with resonator-enhanced measurements.

3.1 Citraconic anhydride

The spectrum of citraconic anhydride showed two lines for each transition, as the vibrational ground state ($v = 0$) is split into two (A and E) C_3 torsional symmetry components due to the presence of an internal methyl rotor, that has a torsional potential energy barrier, which lifts the threefold degeneracy of the C_3 top in the harmonic oscillator limit. An example spectrum for an A/E-splitting is provided in Fig. 2. Because of the presence of an internal rotor, fitting was performed using XIAM by Hartwig and Dreizler,[61] which uses a "combined internal axis method" to fit all the components of the Hamiltonian, which for CA consists of the rigid rotor Hamiltonian $\mathscr{H}_{rr}$, its centrifugal distortion $\mathscr{H}_{cd}$ and the corresponding internal rotor components, $\mathscr{H}_{rr}^{(int.)}$ and $\mathscr{H}_{cd}^{(int.)}$,

$$\mathscr{H} = \mathscr{H}_{rr} + \mathscr{H}_{cd} + \mathscr{H}_{rr}^{(int.)} + \mathscr{H}_{cd}^{(int.)}. \quad (1)$$

The standard rigid rotor Hamiltonian is given by

$$\mathscr{H}_{rr} = B_J P^2 + B_K P_a^2 + B_-(P_b^2 - P_c^2) \quad (2)$$

where all P_g, $g \in \{a,b,c\}$ represent the angular momentum along the different axes and P the total angular momentum. B_J, B_K
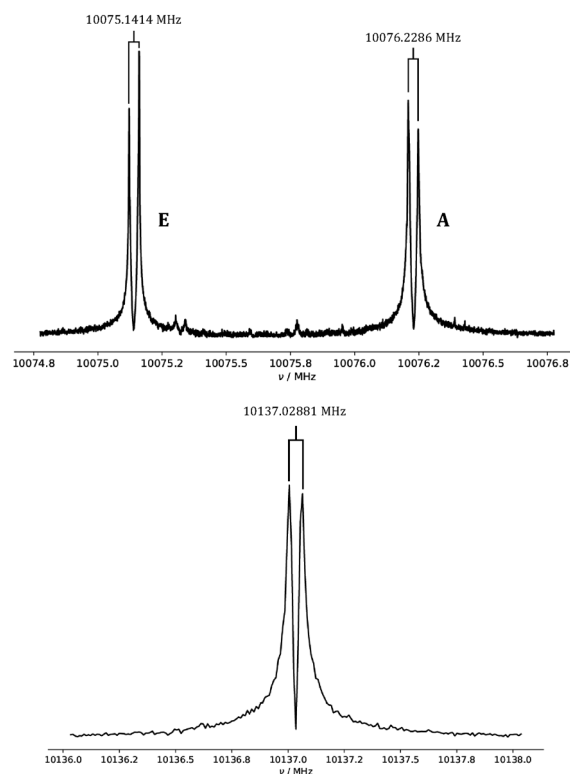

Fig. 2 Experimental spectra of the $3_{1,3} \leftarrow 2_{0,2}$ transition of citraconic anhydride (left) and itaconic anhydride (right). For citraconic anhydride, the transition is split into an A and E torsional symmetry component.

Fig. 1 Labeled structure of citraconic anhydride (CA).

This journal is © the Owner Societies 2025

Phys. Chem. Chem. Phys., 2025, **27**, 9491–9503 | **9493**

and B_- are obtained by a transformation of the rotational constants A, B and C using the following equations:

$$2B_J = B + C \tag{3}$$

$$2B_K = 2A - B - C \tag{4}$$

$$2B_- = B - C \tag{5}$$

The centrifugal distortion Hamiltonian $\mathscr{H}_{cd}$ for terms up to quartic order was used. Sixth order terms were neglected. Using Watson's S reduction,[62] $\mathscr{H}_{cd}$ was reduced to

$$\mathscr{H}_{cd} = -D_J P^4 - D_{JK} P_a^2 P^2 - D_K P_a^4 + d_1 P^2 (P_+^2 + P_-^2) + d_2 (P_+^4 + P_-^4) \tag{6}$$

with $P_\pm = P_x \pm i P_y$ and where all D_h, $h \in \{J, JK, K\}$ are diagonal and δ_i, $i \in \{1,2\}$ off-diagonal quartic centrifugal distortion constants within the symmetrically reduced Hamiltonian. The values of these constants were determined by fitting.

The internal rigid rotor Hamiltonian can be denoted by

$$\mathscr{H}_{rr}^{(int.)} = F(P_\alpha - \rho P_\rho)^2 + V(\alpha) \tag{7}$$

where F is the reduced rotational constant of the methyl top, which was approximated analytically and constrained in the fit. P_α resembles the angular momentum around the methyl top C_3-axis and ρ is the angle between the principal axis system (PAS) and the internal rho axis system (RAS) of the methyl top. The hindering potential $V(\alpha)$ gives the potential energy of the methyl top V with respect to the methyl rotational angle α. $V(\alpha)$ can generally be expressed as

$$2V(\alpha) = \sum_{i=1}^{\infty} V_{i\cdot n}(1 - \cos(in\alpha)) \tag{8}$$

for an n-fold top. In the case of CA, which has a methyl top with $n = 3$ and neglecting terms with $i > 1$, the potential $V(\alpha)$ simplifies to

$$2V(\alpha) = V_3[1 - \cos(3\alpha)]. \tag{9}$$

As only the A/E symmetry species belonging to the same torsional state, $v = 0$, were observed, fits including higher order terms like V_6 do not yield determined results and were not included, leaving the V_3 value being an effective barrier.

Lastly, the methyl top centrifugal distortion Hamiltonian is given by

$$\mathscr{H}_{cd}^{(int.)} = 2D_{\pi2J}(P_\alpha - \rho P_\rho)^2 P^2 + D_{\pi2K}[(P_\alpha - \rho P_\rho)^2 P_a^2 + P_a^2(P_\alpha - \rho P_\rho)^2] \tag{10}$$

Fits did not give well determined results for the internal centrifugal distortion parameters $D_{\pi2-}$ and D_{C_3J}, hence these were not included in the employed Hamiltonian given in eqn (10).

In total, 97 transitions were measured, with 44 pairs of transitions showing A/E-splitting. Nine of the 97 transitions were c-type transitions. Due to the planar symmetry of the molecule, these transitions could only be observed for the excited E-states as no c-type spectrum is observable for $\mu_c = 0$ symmetry forbidden A-states. The least squares fit performed

Table 1 Experimental results for the parent species of citraconic anhydride compared with the computational equilibrium results from DSD-PBEP86. A comparison with all other tested methods can be found in the ESI. The κ refers to Ray's asymmetry parameter, N to the number of lines and σ to the root mean square deviation of the fit. Values in brackets have been kept at the computationally predicted value and values in parentheses are 1σ uncertainties. The value for F was taken from an MP2 optimized geometry

	Experiment	DSD-PBEP86
A/MHz	3914.01207(26)	3927.6311
B/MHz	1886.045890(82)	1888.2051
C/MHz	1282.788828(67)	1285.2118
D_J/kHz	0.0543(12)	0.05492
D_{JK}/kHz	0.0989(29)	0.09249
D_K/kHz	1.488(12)	1.504
d_1/kHz	−0.01952(21)	−0.0196
d_2/kHz	−0.00362(12)	−0.003333
F/GHz	[160.1]	159.9
V_3/cm^{-1}	326.5153(61)	326.58
V_3/kJ mol^{-1}	3.905990(74)	3.9067
$D_{\pi2J}$/MHz	0.00989(87)	—
$D_{\pi2K}$/MHz	−0.1155(29)	—
δ/°	23.909(92)	24.1
$|\mu_a|$/D	Strong	2.58
$|\mu_b|$/D	Very strong	3.99
$|\mu_c|$/D	(See text)	0
κ	−0.54146	−0.54361
N	97	—
σ/kHz	1.56	—

with XIAM resulted in a well determined set of parameters for the parent species, which are presented in Table 1 alongside the theoretical predictions (all reported uncertainties are 1σ uncertainties).

Most notably, the barrier to internal rotation V_3 was determined to be 326.5153(61) cm^{-1} (3.905990(74) kJ mol^{-1}), which as shown in Table 1 is well reproduced by the quantum chemical methods. The potential energy curve $V(\alpha)$ is shown in Fig. 3 for the PBE0 and DSD-PBEP86 DFT methods, the latter using a certain amount of HF exchange from MP2, which itself is also shown. The maximum potential at $\alpha(n) = (2n + 1)\pi/3$, $n \in \mathbb{Z}$ can be rationalized by the electronic repulsion of the in-plane hydrogen to the oxygen lone pair. The determined barrier of 326.5 cm^{-1} is substantially smaller than the barrier of the structurally related s-trans methacrylic acid (MMA) with 611.2 cm^{-1},[63] but higher than V_3 of several acetyl derived compounds, where the V_3 drops with stronger +M substituents at the carbonyl group.[64] This can be explained by stabilizing orbital interactions between σ(C–H) and π^*(C–O) that decrease with stronger +M conjugation. The orbital interactions also explain why the V_3 barrier of MMA is that much higher than that of CA. The distance between O and H atoms is predicted to be about 0.2 Å shorter in MMA due to ring strain, leading to stronger stabilizing interactions and steric hindrance in MMA, resulting in the higher barrier.

For citraconic anhydride, all five ^{13}C and all three ^{18}O mono-substituted isotopologues could be characterised through

9494 | *Phys. Chem. Chem. Phys.*, 2025, **27**, 9491–9503
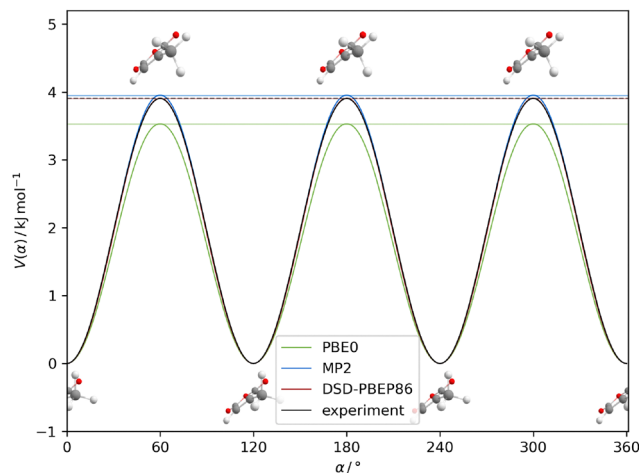
This journal is © the Owner Societies 2025

Fig. 3 Relaxed surface scan with respect to the methyl torsional angle α in kJ mol^{-1} for the experiment compared to the predictions by the PBE0/, MP2/ and DSD-PBEP86/aVTZ levels of theory.

measurements in natural abundance (na). For each ^{13}C isotopologues, 12–16 lines (6–8 transitions) and for each ^{18}O isotopologue, 8 lines (4 transitions) were observed. The resulting rotational constants can be found in the ESI.†

The changes of rotational constants for the isotopologues relative to the parent species allowed for the determination of the molecular structure of the the whole planar carbon–oxygen molecular framework using Kraitchman's equations[65–68] which were solved with Z. Kisiel's KRA (version 4a.IV.2017) program. The coordinates were derived from the rotational constants A, B and C and the reduced change of mass of the molecule upon isotopic substitution. This yielded an experimental r_S substitution structure, that in theory should be closer to the equilibrium structure (r_e) than the experimental vibrational ground state structure (r_0) as vibrational ground state contributions are partially eliminated by taking only the differences in the moments of inertia from the respective isotopologue to its parent species. Alternatively, the vibrational effects can be accounted for by VPT2 calculations so that one obtains equilibrium rotational constants corrected by theory, i.e. semi-experimental equilibrium rotational constants $B_{0\to e}^{SE}$. These corrected constants can then be used to obtain a semi-experimental equilibrium structure $r_{0\to e}^{SE}$ obtained via a least squares fitting routine, rather than using Kraitchman's equation together with the corrected constants, referred to as $r_{0\to e}^{SE}$. The structural fits were conducted with Kisiel's STRFIT program (Version 14.VI.2021).[69] Note that we derive all uncertainties from the xyz-structures provided by STRFIT. The STRFIT and KRA program can be downloaded from the PROSPE (programs for ROtational SPEctroscopy) website.[70]

For the different methods for which VPT2 calculations have been conducted, their respective equilibrium structures were used as an initial input in a z-matrix format. Only bonds and angles that involve atoms for which isotopic data is available were fitted. All distances and angles involving hydrogen atoms remain at their computed equilibrium values. The values found

for each determinable bond length and angle can be found in Table S5 of the ESI.† Note that, cyclic structures only grant $n - 1$ degrees of freedom (DoF) for bond lengths, where n is the number of atoms included in the fit. For bond angles, there are $n - 2$ DoF. Thus, in total, one bond length and five angles presented in the table had to be derived from the coordinates returned by STRFIT. No uncertainties are reported in these cases, as the covariance matrix does not account for the respective parameters.

3.2 Itaconic anhydride

In contrast to citraconic anhydride, itaconic anhydride does not show an A/E splitting, as no internal rotor is present (Fig. 4). An example spectrum of the $3_{1,3} \leftarrow 2_{0,2}$ transition is shown in Fig. 2. Therefore, the Hamiltonian of IA is much simpler than for CA as it only comprises the rigid rotor Hamiltonian $\mathscr{H}_{rr}$ and the centrifugal distortion component $\mathscr{H}_{cd}$. Not having to account for an internal rotor, fitting was carried out using Pickett.[71] With Watson's S reduction being used, $\mathscr{H}_{cd}$ was calculated in the I^r representation as shown in eqn (6). Pickett also fits $\mathscr{H}_{rr}$ as stated in (2), only using the untransformed rotational constants A, B and C. Thus the expression for $\mathscr{H}_{rr}$ may be rewritten as

$$\mathscr{H}_{rr} = AP_a^2 + BP_b^2 + CP_c^2. \quad (11)$$

The results of the fit for the parent species (94.0% na) conducted with Pickett as well as the respective theoretical ab initio calculations are summarized in Table 2.

Like for CA, the r_S structure was determined through isotopic measurements in natural abundance. However, as IA has a much lower vapor pressure, transition intensities only allowed for the measurement of each ^{13}C mono-substituted isotope (1.0%) while for the ^{18}O isotopic species (0.2%) intensities were likely below the noise level. In total, 46 a- and b-type transitions could be observed for the parent species while no c-type spectrum was observed, since $\mu_c = 0$ and no perturbed states were present that could allow for the otherwise dipole
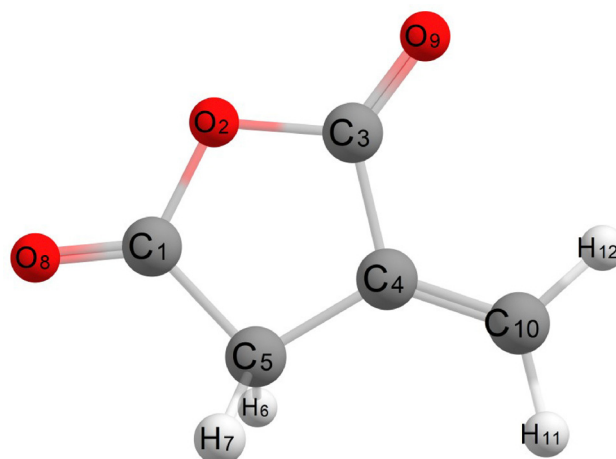

Fig. 4 Labeled structure of itaconic anhydride (IA).

Table 2 Experimental results for the parent species of itaconic anhydride compared with the computational equilibrium results from DSD-PBEP86. A comparison with all other tested methods can be found in the ESI. The κ refers to Ray's asymmetry parameter, N to the number of lines and σ to the root mean square deviation of the fit. Values in parentheses are 1σ uncertainties

	Experiment	DSD-PBEP86
A/MHz	3901.06797(19)	3917.282
B/MHz	1921.85699(17)	1923.36
C/MHz	1298.78883(12)	1300.393
D_J/kHz	0.0573(21)	0.05304
D_{JK}/kHz	0.1212(55)	0.107
D_K/kHz	1.040(11)	1.030
d_1/kHz	−0.0208(12)	−0.01955
d_2/kHz	−0.00393(44)	−0.003961
$|\mu_a|$/Debye	Strong	1.91
$|\mu_b|$/Debye	Strong	4.50
$|\mu_c|$/Debye	None	0
κ	−0.52114	−0.52389
N	46	—
σ/kHz	1.39	—

forbidden transitions. For the mono-substituted ^{13}C isotopologues 7–8 transitions were measured, which for every isotopologue yielded very low σ fits at $\sigma < 1.30$ kHz for the rotational constants A, B and C. The individual rotational constants can be found in the ESI.†

From the rotational constants, the r_S coordinates for all carbon atoms were derived *via* Kraitchman's equations. As for citraconic anhydride, the r_S structure was compared to the $r_{0 \to e}^{SE}$ structures using the same theoretical methods to make up for vibrational contributions to the rotational constants of the r_0 structure. As the rotational constants for the ^{18}O isotopes were not determined, fewer bond lengths and angles could be fit with STRFIT. The results of the structure fitting for all tested methods and the r_S values can be found in Table S7 of the ESI.†

4 Discussion

In the following, structural comparisons of CA and IA are discussed along with their relative stability and isomerization prospects.

4.1 Structure determination

For both compounds, isotopic measurements in natural abundance allowed for the determination of an r_S structure, which was compared to the semi-experimental equilibrium structures ($r_{0 \to e}^{SE}$) using different computational methods. The raw structural data of the r_S and $r_{0 \to e}^{SE}$ structures can be found in the ESI.† For the purpose of structural comparisons, we used the CCSD(T) equilibrium structure as a reference as it is often referred to as the "gold standard" and is expected to be the most accurate method. Our obtained structural parameters from the $r_{0 \to e}^{SE}$ fits can then be directly compared to the CCSD(T) values. In addition, we also compare the DCSD r_e structure to CCSD(T) in order to test its accuracy and to explore

its possibility as a cheaper but accurate option to CCSD(T). The methods were evaluated using the relative deviation of fitted bond lengths d_i^{rel} and angles $\angle_i^{rel}$ to the ones computed with CCSD(T) for both compounds separately with n data points for every method. To compare the relative deviations to each other, a root mean square deviation (RMSD) with n DoF was used alongside the signed median absolute deviation (SMAD). Here, signed refers to the fact that the sign of the median deviation is kept so that the SMAD still reflects the positive or negative tendency of the median. The comparison between CCSD(T) and DCSD was limited to the bond lengths and angles also obtained with the $r_{0 \to e}^{SE}$ fits.

In Fig. 5 and 6 the median (green) and standard deviation (blue) of the relative deviations to the CCSD(T) geometry are shown for CA and IA, respectively. Due to the deviations being in different orders of magnitude, varying scales were used in the figures. Bond angles were generally better reproduced by all methods than the bond lengths. As can be seen, DCSD outperforms all other tested methods in this comparison and can indeed be regarded as a computationally less expensive substitute for CCSD(T). Curiously, MP2, which comes at a similar
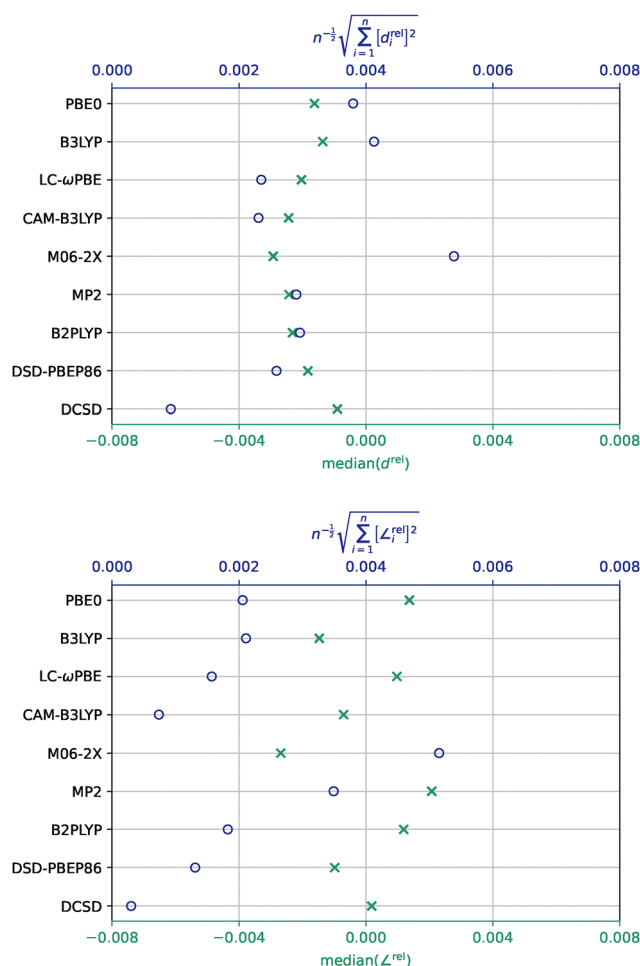
Fig. 5 Comparison of standard and median deviations of bond lengths d^{rel} (above) and angles $\angle^{rel}$ (below) from CCSD(T) for all $r_{0 \to e}^{SE}$ structures in citraconic anhydride (8 and 11 data points).

9496 | *Phys. Chem. Chem. Phys.*, 2025, **27**, 9491–9503
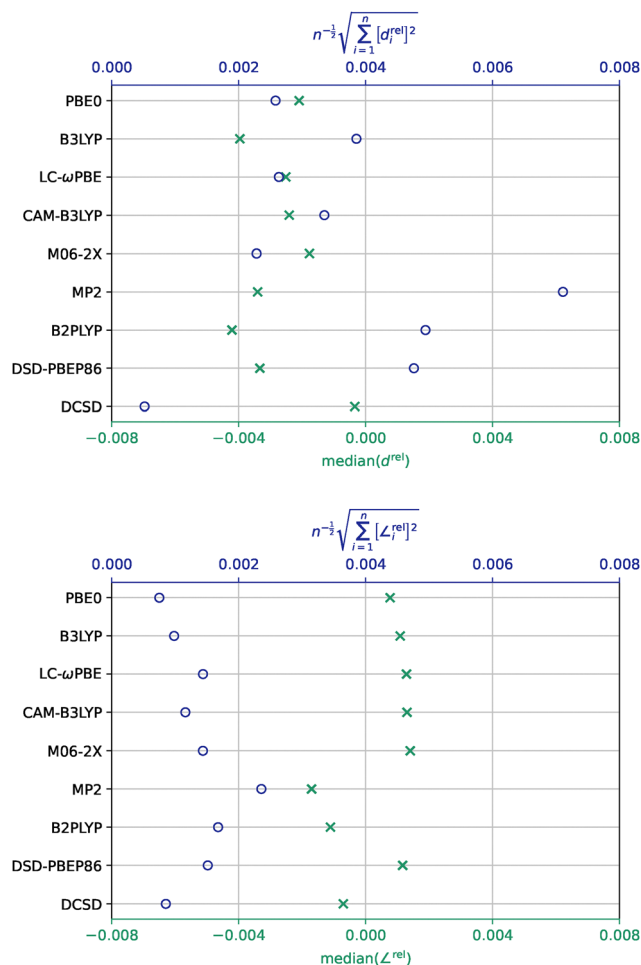
This journal is © the Owner Societies 2025

Fig. 6 Comparison of standard and median deviations of bond lengths d^{rel} (above) and angles $\angle^{rel}$ (below) from CCSD(T) for all $r_{0\to e}^{SE}$ structures in itaconic anhydride (4 and 4 data points).

cost to B2PLYP and DSD-PBEP86, performs the worst out of all the methods for IA relative to CCSD(T). On the other hand, M06-2X, which comes at a similar cost to CAM-B3LYP and LC-ωPBE, shows the worst agreement with CCSD(T) for CA of all tested methods. These conclusions are primarily drawn from the RMSD, but can also be observed in the SMAD. The computational differences might be attributed to fewer data points being available for IA in comparison to CA, which is a byproduct of fewer isotopologue measurements conducted in natural abundance. However, the comparisons might also be influenced by the fixed values from the $r_{0\to e}^{SE}$ input structures such as the C–H bond lengths, which would take away some of the meaningfulness of the fit.

In total, no method clearly performs the second-best behind DCSD, however, PBE0 and CAM-B3LYP yield good results, *i.e.* they reproduce the CCSD(T) values accurately at a low computational cost. Of the significantly more expensive methods involving corrections based on MP2 and MP2 itself, DSD-PBEP86 performs the best.

The fitting uncertainties σ_{fit} for CA vary significantly between the different methods, ranging from 0.042 MHz up to 0.200 MHz

(see Table S5 of the ESI†). The fitting uncertainties for the more expensive DSD-PBEP86 (σ_{fit} = 0.042 MHz) and MP2 (σ_{fit} = 0.049 MHz) are especially low. The highest uncertainties were observed for B3LYP (σ_{fit} = 0.174 MHz) and CAM-B3LYP (σ_{fit} = 0.200 MHz). For IA, due to fewer datapoints, σ_{fit} is generally higher and fluctuates more strongly between the methods when compared to CA. σ_{fit} ranges from 0.107 MHz to 0.398 MHz (see Table S7 of the ESI†). DSD-PBEP86 remains the best performer with an uncertainty of 0.107 MHz, while CAM-B3LYP (σ_{fit} = 0.398 MHz) and B3LYP (σ_{fit} = 0.374 MHz) show the highest σ_{fit}. All other methods yield results that exceed the previous largest uncertainties of CA. Considering σ_{fit} and the structural differences to the CCSD(T) geometry, discussed in the previous paragraph, DSD-PBEP86 yields the best results, performing well in either case. From the previously mentioned computationally less expensive methods, LC-ωPBE and PBE0 should be preferred over CAM-B3LYP and B3LYP, because they both yield a lower σ_{fit}.

Complementary to the $r_{0\to e}^{SE}$ geometries, $r_m^{(1)}$ and $r_m^{(2)}$ structures were determined with the measured rotational constants. These fits use empirical correction parameters c_g, $g \in \{a,b,c\}$ in the case of $r_m^{(1)}$ with the addition of d_g in case of $r_m^{(2)}$ to assess vibrational contributions to the ground state structure. This correction was initially proposed by Watson *et al.*[72] and can be described by eqn (12), where I_0^g is the measured moment of inertia to the respective axis and I_m^g its rigid frame contribution, while the m_i represent the masses of all n atoms and M the molecular mass of the respective isotopologue.

$$I_0^g = I_m^g + c_g\left(I_m^g\right)^{1/2} + d_g\left(\prod_{i=1}^n m_i/M\right)^{1/(2n-2)} \quad (12)$$

The obtained structures were also assessed in terms of their σ_{fit} and their geometrical similarity to the CCSD(T) r_e structure in terms of bond lengths and angles. A comparison between the CCSD(T) r_e geometry and the $r_m^{(2)}$ structures, similar to those previously done for the $r_{0\to e}^{SE}$ results, are shown in Fig. 7 and 8. The respective $r_m^{(1)}$ comparisons can be found in the ESI.† As can be seen in the figures, all methods converged to similar results for CA, with only the median of the B3LYP angle deviation showing a different tendency from the other methods, which is a statistical artefact. For CA, the $r_m^{(2)}$ fits generally produced more accurate geometries than the $r_m^{(1)}$ fits. This tendency is not reflected in the σ_{fit} values, which were generally higher for the $r_m^{(2)}$ fits. The σ_{fit} values were very close between all methods, however, PBE0 showed the highest $r_m^{(2)}$ σ_{fit} at 0.0449 MHz while DSD-PBEP86 had the lowest σ_{fit} at 0.0411 MHz. For IA, the differences between the methods is not as subtle as for CA. Here, DSD-PBEP86 stands out again to reproduce the CCSD(T) geometry the best, closely followed by MP2. From the less expensive DFT functionals, PBE0 performs the best. The respective $r_m^{(1)}$ fits yielded lower deviations from the CCSD(T) geometry but much higher σ_{fit} values, which can be explained by the ratio of fitted parameters to rotational constants. For the CA $r_m^{(1)}$ structure, 16 parameters were fit with 24 rotational constants, yielding a ratio of 0.67, while for the $r_m^{(2)}$ fits a ratio of 0.79 (19/24) can be obtained, still giving a well determined fit.
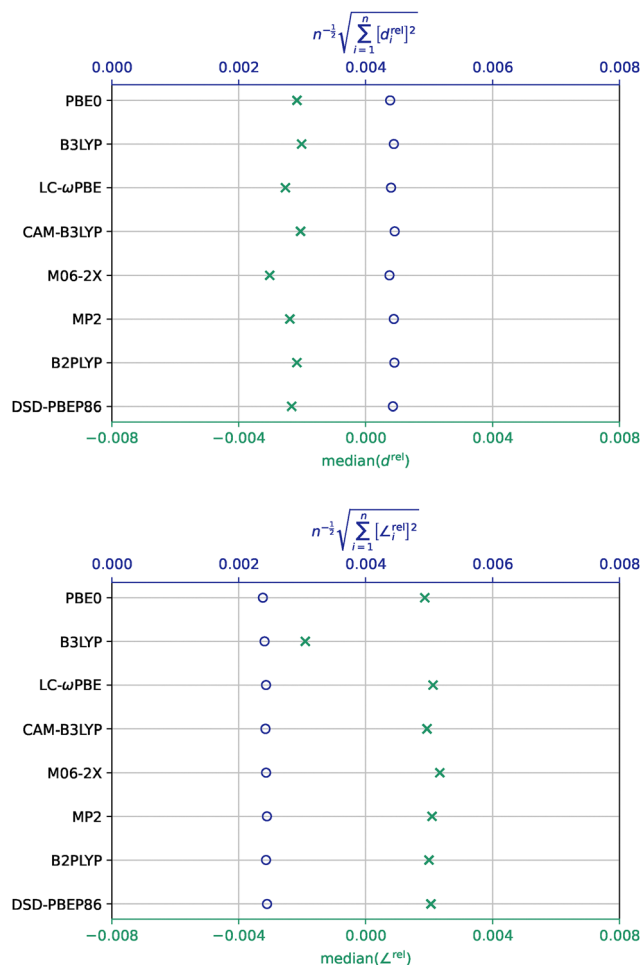
Fig. 7 Comparison of standard and median deviations of bond lengths d^{rel} (above) and angles $\angle^{rel}$ (below) from CCSD(T) for all $r_m^{(2)}$ structures in citraconic anhydride (8 and 11 data points).

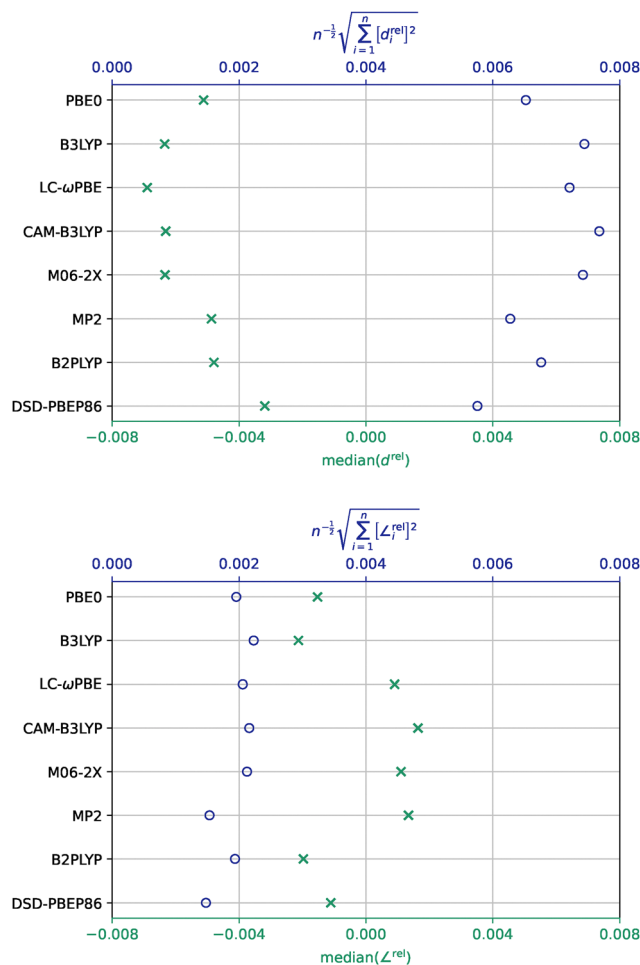**Fig. 8** Comparison of standard and median deviations of bond lengths d^{rel} (above) and angles $\angle^{rel}$ (below) from CCSD(T) for all $r_m^{(2)}$ structures in itaconic anhydride (4 and 4 data points).

However, for IA, ratios of 0.67 (10/15) and 0.87 (13/15) were obtained for $r_m^{(1)}$ and $r_m^{(2)}$, respectively. The latter case is only slightly over-determined and thus yields a higher geometric deviation to CCSD(T). Here, the MP2 assisted DFT functionals DSD-PBEP86 and B2PLYP along with MP2 itself showed the lowest σ_{fit} on average, while LC-ωPBE and M06-2X had the highest σ_{fit} for both $r_m^{(1)}$ and $r_m^{(2)}$.

All fit-determined $r_{0\to e}^{SE}$, $r_m^{(1)}$ and $r_m^{(2)}$ geometries correlate well with the predicted r_e geometry of CCSD(T) as well as the r_S structure, which allow us to draw direct conclusions about the position of the C=C double bond linked to the rotational constants of the respective parent species. The shortest C–C distance was found to be between the C_5 and C_4 for CA ($d(r_S)$ = 1.32747(51) Å) and between the C_4 and C_{10} atoms for IA ($d(r_S)$ = 1.3376(47) Å), as one would expect for the respective molecules. A side by side comparison of CA and IA with all (semi)-experimentally determined bond distances as well as computed equilibrium values at the CCSD(T) level of theory are shown in Fig. 9. We also find that the single bonds involving the sp^3 hybridized carbon atom are longer (C_1–C_5 and C_4–C_5 for IA and C_4–C_9 for CA) than the other sp^2–sp^2 C–C single bonds, typical for such systems. The difference in the bond length of C_1–C_5

between CA and IA can be rationalized by differences in the π-delocalization since the C_5 atom in CA is part of the π-system whereas in IA sp^3-hybridization prevents it from resonance with the π-system. The shorter bond length of C_3–C_4 in IA may also be explained in light of its decreased delocalization which leads to an increase of electron density at the C_4-atom which in turn allows for a stronger double bond character for the C_3–C_4 bond. In addition, differences in ring strain may also provide an adequate explanation. The ring strain is more pronounced in CA as indicated by $\angle(C_1$–C_5–$C_4)$ which is much closer to its ideal angle in IA (Exp.: ca. 103.2° vs. ideal: 109.5°) than in CA (Exp.: ca. 108.5° vs. ideal: 120.0°). This decrease could then allow for a better orbital overlap in the IA case for the C_3–C_4 bond. Unfortunately, these two effects cannot be readily separated and it is unclear which effect might dominate.

We may also compare our determined structures with the $r_{0\to e}^{SE}$ structures obtained for maleic[73] and succinic anhydride.[74] In the case of maleic anhydride, good agreement is expected for CA, whereas for succinic anhydride partially better agreement is expected for IA. We indeed observe this behaviour with bond distances away from the methyl/methylene group being a better
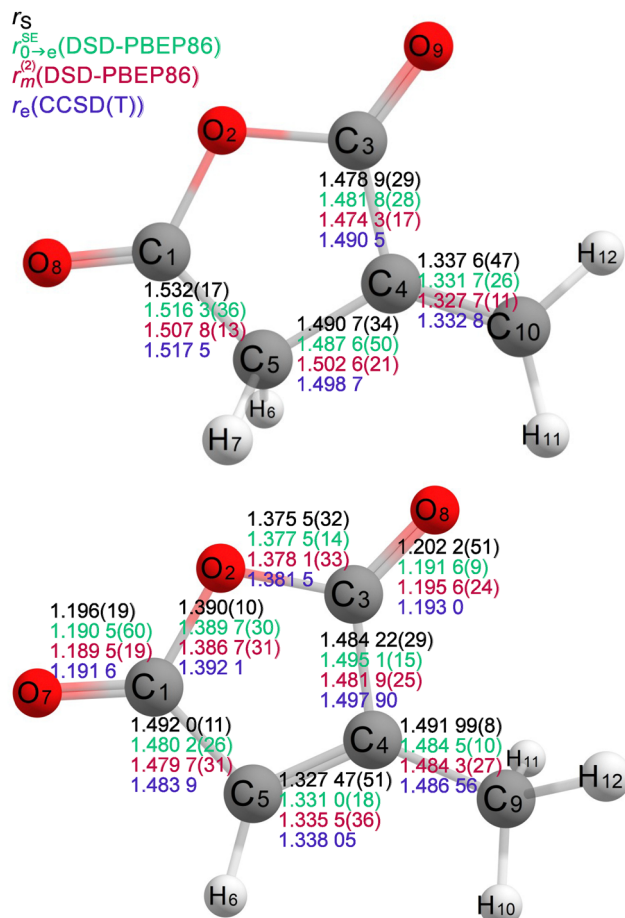
9498 | *Phys. Chem. Chem. Phys.*, 2025, **27**, 9491–9503

This journal is © the Owner Societies 2025

r_S
$r_{0\rightarrow e}^{SE}$(DSD-PBEP86)
$r_m^{(2)}$(DSD-PBEP86)
r_e(CCSD(T))

Fig. 9 Comparison of the bond distances of itaconic anhydride (top) and citraconic anhydride (bottom) from Kraitchman's substitution structure (black), a semi experimental equilibrium structure (green) as well as mass dependent $r_m^{(2)}$ (red) using DSD-PBEP86 and an equilibrium structure at the CCSD(T) level of theory (purple). All values are given in Å.

match between CA and maleic anhydride as well as IA and succinic anhydride. For CA, this also applies to the C=O and C–O bonds. A detailed comparison of the four structures can be found in the ESI† (Fig. S2).

Drawing from the bonding information, we found that the previously reported rotational spectrum of IA[9] actually shows better agreement with our CA characterization. Most notably, in the rotational spectrum, two lines were observed for each transition which was attributed to ground and excited vibrational state with (+, −)-symmetry where the excited state was believed to be a ring puckering motion. The symmetric (0^+) and anti-symmetric (0^-) vibrational states of IA were fitted separately. However, they could not observe any c-type transitions, which prevented them from fitting any Coriolis coupling constants F_{ij}. The resulting fits yielded high uncertainties. While we also looked for a 0^+ and 0^- splitting in the IA spectrum, our *ab initio* calculations and CA measurements suggest that the 0^+ and 0^- fits reported in their study are actually fits of CA, where their observed splitting was caused by the A/E-splitting of the C_3 methyl top rotation. Their assigned torsional subbands of the

Table 3 Calculated activation energies $\Delta G^{\ddagger}$, imaginary transition state frequencies $\tilde{\nu}_{ts}$ and isomerization enthalpies ΔH_{iso} for different functionals at 0 K. Values for $\Delta G^{\ddagger}$ as well ΔH_{iso} are given in kJ mol^{-1} and $\tilde{\nu}_{ts}$ in i cm^{-1}

	$\Delta G^{\ddagger}$	$\tilde{\nu}_{ts}$	ΔH_{iso}	$\Delta G^{\ddagger}/\Delta H_{iso}$
B3LYP	362.4	1773	19.3	18.78
PBE0	353.2	1827	20.9	17.87
CAM-B3LYP	377.0	1889	17.9	21.09
LC-wPBE	379.5	1946	17.2	22.03
M06-2X	372.1	1867	18.4	20.17
B2PLYP	365.4	1858	21.2	17.23
DSD-PBEP86	367.7	1904	21.5	17.08
MP2	358.7	1894	23.2	15.46

$3_{1,3} \leftarrow 2_{0,2}$ transition§ of IA shown in Fig. 3(b) of ref. 9 actually corresponds to the $3_{1,3} \leftarrow 2_{0,2}$ transition of CA shown in Fig. 2. The same transition for IA is also shown exhibiting no splitting. Given the large $|\mu_b|$ (see Table S1 of the ESI†), this transition is particularly intense. Moreover, the D_K distortion constant varies significantly between IA (D_K = 1.040(11) kHz) and CA (D_K = 1.488(12) kHz) which is accurately predicted by the VPT2 calculations (see Table S1 of the ESI†) again supporting this interpretation.

4.2 Isomerization prospects

In the study of McMahon *et al.*,[9] the anhydride was synthesized *in situ* from itaconic acid *via* thermal dehydration at 403 K (130 °C). The fact that they still observed CA led us to take a closer look at the equilibrium of CA and IA.

Test measurements revealed, that CA is in fact present in our IA spectrum while only trace amounts of IA could be observed in the CA spectrum. The CA signal intensity in the IA spectrum increased over time when the same sample was used, indicating thermal conversion of IA to CA. The IA signals in the CA spectrum, on the other hand, were weak and did not change significantly over time. The mutual presence in each other's spectrum is to be expected, as the molecules are not only constitutional isomers but also tautomers since they can convert into each other by the transfer of a hydrogen atom from IA's C_5 to CA's C_9 atom or *vice versa*. The question then comes as to if this tautomerization occurs in the gas phase. To understand the isomerization in the gas phase, we computed the transition state of the conversion at different levels of theory. The presence of a transition state was confirmed by a single imaginary frequency being present in all cases. The results are shown in Table 3. Note that all values have been computed at 0 K so that the enthalpy of isomerization ΔH_{iso} is equal to the zero point corrected relative energies ΔE_0 and the Gibbs energy of activation $\Delta G^{\ddagger}$ to the zero-point corrected energy difference between IA and the transition state. The barriers are consistently very high ranging from 350–380 kJ mol^{-1} for the conversion of the less stable IA to the more stable CA. In our microwave experiments with IA the nozzle reservoir has been heated to at most 373 K (100 °C) resulting in a thermal energy of about 3 kJ mol^{-1}. Hence, isomerization in the gas phase appears

§ This transition is labeled as $4_{1,3} \leftarrow 2_{0,2}$ in the original work's caption, which is probably a typing error as this would be a dipole forbidden transition.

This journal is © the Owner Societies 2025

Phys. Chem. Chem. Phys., 2025, **27**, 9491–9503 | **9499**

to be very unlikely. However, isomerization may be possible in the solid sample itself and may be significantly enhanced in the molten state.

Experimentally, ΔH_{iso} can be obtained using van't Hoff's equation. For this purpose, temperature dependent measurements have been conducted for both the IA and CA samples. This approach would require a temperature dependent calculation of the tautomerization constant K which is proportional to the relative intensities I of the same rotational transitions in the gas phase, scaled by the reciprocal dipole moment ratio of the corresponding transition μ_g, $g \in a,b$ as stated in (13), assuming a $\pi/2$ pulse.

$$K = \lambda \cdot \frac{I(CA)}{I(IA)} \cdot \frac{\mu_g(IA)}{\mu_g(CA)} \tag{13}$$

where λ is a temperature independent proportionality constant. This proportionality would allow for a determination of the temperature averaged $\langle \Delta H_{iso} \rangle$ via

$$\langle \Delta H_{iso} \rangle = -R \cdot \frac{d \ln K}{d T^{-1}} \tag{14}$$

with the universal gas constant R. Equations like (14) are common and also employed for enthalpy assessments or vapor pressure extrapolations using the Clausius–Clapeyron-equation. In our case, this expression is useful in the sense, that the derivative of the logarithmic equilibrium constant with respect to T^{-1} is not dependent on λ. For μ_g ab initio calculations could be used, but also an experimental determination by the use of the Stark effect would be imaginable.

However no linear increase of $\ln K$ with respect to T^{-1} could be observed, but rather inconsistent tendencies in the relative intensities leading to the conclusion that CA and IA are not in tautomeric equilibrium in the gas phase.

Now, as the experimental setup apparently did not allow for the equilibrium to be reached, other methods were used to explore the possibility of isomerization. Most promisingly, Raman spectroscopy using a curry-jet setup which has been described in ref. 75–77 was employed. The advantage of this experimental setup was the presence of a separate heatable saturator, which in principle allows heating up to 393 K (120 °C). In our testing it was kept at 343 K (70 °C) for IA and 313 K (40 °C) for CA. The tubing behind the saturator (ca. 2.5 m) was heated to at most 463 K (190 °C) to promote the conversion. However, no evidence of gas-phase isomerization could be observed, even in the presence of tertiary amines like N,N-dimethylaniline, which previously were reported to catalyze IA–CA-tautomerization.[78]

Coming back to the study of McMahon et al., we discuss the isomerization process and the differences between the gas phase and liquid phase in more detail. While we measured the commercial samples of the anhydrides, they used itaconic acid and converted it in situ to their anhydrides using thermal dehydration by heating them to 403 K (130 °C).[9] This process opens avenues for acid assisted proton transfers through an allylic carbanion intermediate as illustrated in (10), which could catalyze the process by lowering the barrier through an
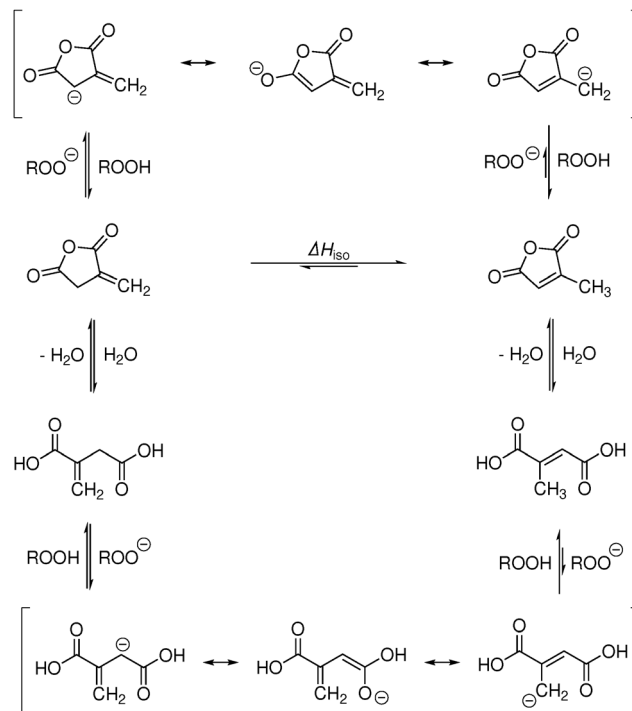

Fig. 10 Possible tautomerization pathways from IA to CA through a resonance stabilised carbanion intermediate.

intermolecular process in the liquid phase due to solvation. In the gas phase the process has to be intramolecular, i.e. direct. Additionally, liquid-phase dynamics make this process much more likely than isolated gas-phase events. However, it remains unclear if the isomerization primarily takes place in the acid or anhydride form or to the same extent in both (Fig. 10).

Future experiments using solvent assisted proton transfers are planned which would enable the thermodynamical equilibration and allowing for more consistent temperature dependent tautomerization constant measurements. Approaches involve preparing samples at different temperatures with different protic solvents or tertiary amines and allowing for the thermodynamical equilibration before measuring. With the estimated isomerization enthalpies and neglecting entropic contributions, which would most likely also favor citraconic anhydride, the equilibrium would be heavily on the side of CA assuming a Boltzmann distribution ($K \approx 3 \times 10^3$ at room temperature). This could make measurements challenging, as the spectroscopic sensitivity of IA is also lower in our experiment than that of CA.

5 Summary and conclusions

Both citraconic anhydride (CA) and itaconic anhydride (IA) were characterised by microwave spectroscopy and both molecular structures could be determined by mono-substituted isotopologue measurements in natural abundance. For IA, all five ^{13}C isotopologues were observed and for CA, all five ^{13}C and

9500 | Phys. Chem. Chem. Phys., 2025, **27**, 9491–9503

This journal is © the Owner Societies 2025

all three ^{18}O species were characterised. While the previous study of McMahon *et al.*[9] focused on the microwave spectrum of IA, our measurements revealed, that they in fact observed CA rather than IA. This is confirmed by the accurately determined molecular structures in this paper. Also, the sensitivity of CA in a gas-phase experiment is much higher than that of IA, owing to the much higher vapor pressure. While the spectra differ between the tautomers, the rotational constants are similar, making a misassignment reasonable. McMahon *et al.*[9] attributed an observed line splitting to the vibrational ground and excited ring puckering states, however this should be attributed to the A/E splitting pattern of citraconic anhydride due to the presence of the internal methyl top rotor. Additionally, the V_3 barrier of internal rotation of CA that led to this splitting was found to be 326.5153(61) cm^{-1} (3.905990(74) kJ mol^{-1}).

Attempts to observe an intramolecular gas phase isomerization between the two tautomers were unsuccessful. While some evidence for isomerization could be gathered in the spectra, no consistent tendencies for temperature-dependent measurements were found, which is explained by the high transition state barrier for intramolecular isomerization calculated by various DFT/MP2 methods at around 370 kJ mol^{-1}. Future measurements will use approaches like pre-experimental rather than *in situ* equilibration. This could include samples, that were prepared in the liquid phase beforehand in the presence of tertiary amines and left to stand until equilibration. These would then be measured in the gas phase using the experimental setups already described.

As for theoretical benchmarking of the determined $r_{0 \to e}^{SE}$, $r_m^{(1)}$ and $r_m^{(2)}$ structures relative to the r_e geometry of CCSD(T), DSD-PBEP86 performed the best out of the more expensive methods used, yielding a low σ_{fit} for all geometries. As for the cheaper methods, PBE0 performed best, especially relative to its cost, while also showing a good agreement with the CCSD(T) r_e geometry, even beating the ever popular B3LYP functional. The MP2 method, which comes at a similar cost to DSD-PBEP86, yielded good results for the $r_m^{(2)}$ fits but performed the worst out of every method for the r_e^{SE} geometry of IA, while the M06-2X functional, which comes at a similar cost to CAM-B3LYP and LC-ωPBE and by design should include dispersion corrections, shows the worst agreement with CCSD(T) on the CA geometry. The r_e geometry of DCSD was always very close to CCSD(T) which was more pronounced for the relative deviations in CA. So, in summary, DCSD can be seen as a cheaper alternative to CCSD(T), while DSD-PBEP86 and PBE0 also work well for this set of molecules.

Data availability

Additional data is made avaible in separate data repositories. They include the raw microwave spectra (**https://doi.org/10.25625/FQCEVB**), all computational outputs (**https://doi.org/10.25625/IBKABW**) as well as the outputs of the experimental and structure fits (**https://doi.org/10.25625/AFCLSC**) are provided.[79–81]

Conflicts of interest

The authors have no conflicts of interest to declare.

Acknowledgements

References

1 O. Diels and K. Alder, *Liebigs Ann.*, 1928, **460**, 98–122.

2 K. Kameo, K. Ogawa, K. Takeshita, S. Nakaike, K. Tomisawa and K. Sota, *Chem. Pharm. Bull.*, 1988, **36**, 2050–2060.

3 S. Dinçer, V. Köseli, H. Kesim, Z. M. Rzaev and E. Pişkin, *Eur. Polym. J.*, 2002, **38**, 2143–2152.

4 H. Dixon and R. Perham, *Biochem. J.*, 1968, **109**, 312.

5 M. Atassi and A. Habeeb, *Methods in enzymology*, Elsevier, 1972, vol. 25, pp. 546–553.

6 V. Pfeifer, C. Vojnovich and E. Heger, *Ind. Eng. Chem.*, 1952, **44**, 2975–2980.

7 R. L. Shriner, S. G. Ford and L. J. Roll, *Citraconic Anhydride and Citraconic Acid*, John Wiley & Sons, Ltd, 2003, pp. 28.

8 R. L. Shriner, S. G. Ford and L. J. Roll, *Itaconic Anhydride and Itaconic Acid*, John Wiley & Sons, Ltd, 2003, pp. 70.

9 T. J. McMahon, J. R. Bailey and R. G. Bird, *J. Mol. Spectrosc.*, 2018, **347**, 35–40.

10 V. M. Akhmedov and S. H. Al-Khowaiter, *Catal. Rev.:Sci. Eng.*, 2007, **49**, 33–139.

11 C. A. Dim, C. Sorrells, A. O. Hernandez-Castillo and K. N. Crabtree, *J. Phys. Chem. A*, 2024, **128**, 9754–9762.

12 M. K. Jahn, D. A. Dewald, D. Wachsmuth, J. U. Grabow and S. C. Mehrotra, *J. Mol. Spectrosc.*, 2012, **280**, 54–60.

13 U. Andresen, H. Dreizler, U. Kretschmer, W. Stahl and C. Thomsen, *Fresenius' J. Anal. Chem.*, 1994, **349**, 272–276.

14 M. Schnell, D. Banser and J. U. Grabow, *Rev. Sci. Instrum.*, 2004, **75**, 2111–2115.

15 M. J. Frisch, G. W. Trucks, H. B. Schlegel, G. E. Scuseria, M. A. Robb, J. R. Cheeseman, G. Scalmani, V. Barone, G. A. Petersson, H. Nakatsuji, X. Li, M. Caricato, A. V. Marenich, J. Bloino, B. G. Janesko, R. Gomperts, B. Mennucci,

This journal is © the Owner Societies 2025

Phys. Chem. Chem. Phys., 2025, **27**, 9491–9503 | **9501**

H. P. Hratchian, J. V. Ortiz, A. F. Izmaylov, J. L. Sonnenberg, D. Williams-Young, F. Ding, F. Lipparini, F. Egidi, J. Goings, B. Peng, A. Petrone, T. Henderson, D. Ranasinghe, V. G. Zakrzewski, J. Gao, N. Rega, G. Zheng, W. Liang, M. Hada, M. Ehara, K. Toyota, R. Fukuda, J. Hasegawa, M. Ishida, T. Nakajima, Y. Honda, O. Kitao, H. Nakai, T. Vreven, K. Throssell, J. A. Montgomery, Jr., J. E. Peralta, F. Ogliaro, M. J. Bearpark, J. J. Heyd, E. N. Brothers, K. N. Kudin, V. N. Staroverov, T. A. Keith, R. Kobayashi, J. Normand, K. Raghavachari, A. P. Rendell, J. C. Burant, S. S. Iyengar, J. Tomasi, M. Cossi, J. M. Millam, M. Klene, C. Adamo, R. Cammi, J. W. Ochterski, R. L. Martin, K. Morokuma, O. Farkas, J. B. Foresman and D. J. Fox, *Gaussian 16 Revision C.01*, Gaussian Inc., Wallingford, CT, 2016.

16 H.-J. Werner, P. J. Knowles, G. Knizia, F. R. Manby and M. Schütz, *Wiley Interdiscip. Rev.:Comput. Mol. Sci.*, 2012, **2**, 242–253.

17 H.-J. Werner, P. J. Knowles, F. R. Manby, J. A. Black, K. Doll, A. Heßelmann, D. Kats, A. Köhn, T. Korona, D. A. Kreplin, Q. Ma, T. F. Miller, A. Mitrushchenkov, K. A. Peterson, I. Polyak, G. Rauhut and M. Sibaev, *J. Chem. Phys.*, 2020, **152**, 144107.

18 H.-J. Werner, P. J. Knowles, P. C. W. Györffy, A. Hesselmann, D. Kats, G. Knizia, A. Köhn, T. Korona, D. Kreplin, R. Lindh, Q. Ma, F. R. Manby, A. Mitrushenkov, G. Rauhut, M. Schütz, K. R. Shamasundar, T. B. Adler, R. D. Amos, J. Baker, S. J. Bennie, A. Bernhardsson, A. Berning, J. A. Black, P. J. Bygrave, R. Cimiraglia, D. L. Cooper, D. Coughtrie, M. J. O. Deegan, A. J. Dobbyn, K. Doll, M. Dornbach, F. Eckert, S. Erfort, E. Goll, C. Hampel, G. Hetzer, J. G. Hill, M. Hodges, T. Hrenar, G. Jansen, C. Köppl, C. Kollmar, S. J. R. Lee, Y. Liu, A. W. Lloyd, R. A. Mata, A. J. May, B. Mussard, S. J. McNicholas, W. Meyer, T. F. M. III, M. E. Mura, A. Nicklass, D. P. O'Neill, P. Palmieri, D. Peng, K. A. Peterson, K. Pflüger, R. Pitzer, I. Polyak, P. Pulay, M. Reiher, J. O. Richardson, J. B. Robinson, B. Schröder, M. Schwilk, T. Shiozaki, M. Sibaev, H. Stoll, A. J. Stone, R. Tarroni, T. Thorsteinsson, J. Toulouse, M. Wang, M. Welborn and B. Ziegler, *MOLPRO, version 2022.3, a package of ab initio programs*, 2022, see **https://www.molpro.net**.

19 C. Møller and M. S. Plesset, *Phys. Rev.*, 1934, **46**, 618.

20 M. J. Frisch, M. Head-Gordon and J. A. Pople, *Chem. Phys. Lett.*, 1990, **166**, 275–280.

21 M. J. Frisch, M. Head-Gordon and J. A. Pople, *Chem. Phys. Lett.*, 1990, **166**, 281–289.

22 M. Head-Gordon, J. A. Pople and M. J. Frisch, *Chem. Phys. Lett.*, 1988, **153**, 503–506.

23 S. Sæbø and J. Almlöf, *Chem. Phys. Lett.*, 1989, **154**, 83–89.

24 M. Head-Gordon and T. Head-Gordon, *Chem. Phys. Lett.*, 1994, **220**, 122–128.

25 C. Adamo and V. Barone, *J. Chem. Phys.*, 1999, **110**, 6158–6170.

26 M. Enzerhof and G. E. Scuseria, *J. Chem. Phys.*, 1999, **110**, 5029–5036.

27 A. D. Becke, *Opt. Phys.*, 1988, **38**, 3098–3100.

28 C. Lee, W. Yang and R. G. Parr, *Phys. Rev. B:Condens. Matter Mater. Phys.*, 1988, **37**, 785.

29 B. Miehlich, A. Savin, H. Stoll and H. Preuss, *Chem. Phys. Lett.*, 1989, **157**, 200–206.

30 A. D. Becke, *J. Chem. Phys.*, 1993, **98**, 5648–5652.

31 T. Yanai, D. P. Tew and N. C. Handy, *Chem. Phys. Lett.*, 2004, **393**, 51–57.

32 H. Iikura, T. Tsuneda, T. Yanai and K. Hirao, *J. Chem. Phys.*, 2001, **115**, 3540–3544.

33 O. A. Vydrov and G. E. Scuseria, *J. Chem. Phys.*, 2006, **125**, 234109.

34 O. A. Vydrov, J. Heyd, A. V. Krukau and G. E. Scuseria, *J. Chem. Phys.*, 2006, **125**, 074106.

35 Y. Zhao and D. G. Truhlar, *Theor. Chem. Acc.*, 2008, **120**, 215–241.

36 S. Kozuch and J. M. Martin, *Phys. Chem. Chem. Phys.*, 2011, **13**, 20104–20107.

37 S. Kozuch and J. M. Martin, *J. Comput. Chem.*, 2013, **34**, 2327–2344.

38 S. Grimme, *J. Chem. Phys.*, 2006, **124**, 034108.

39 T. Schwabe and S. Grimme, *Phys. Chem. Chem. Phys.*, 2007, **9**, 3397–3406.

40 S. Grimme, *J. Chem. Phys.*, 2003, **118**, 9095–9102.

41 T. H. Dunning Jr, *J. Chem. Phys.*, 1989, **90**, 1007–1023.

42 R. A. Kendall, T. H. Dunning and R. J. Harrison, *J. Chem. Phys.*, 1992, **96**, 6796–6806.

43 S. Grimme, J. Antony, S. Ehrlich and H. Krieg, *J. Chem. Phys.*, 2010, **132**, 154104.

44 S. Grimme, S. Ehrlich and L. Goerigk, *J. Comput. Chem.*, 2011, **32**, 1456–1465.

45 H. H. Nielsen, *Rev. Mod. Phys.*, 1951, **23**, 90–136.

46 V. Barone, *et al.*, *J. Chem. Phys.*, 2005, **122**, 14108.

47 V. Barone, J. Bloino, C. A. Guido and F. Lipparini, *Chem. Phys. Lett.*, 2010, **496**, 157–161.

48 J. Čížek, *J. Chem. Phys.*, 1966, **45**, 4256–4266.

49 J. Čížek, *Adv. Chem. Phys.*, 1969, **14**, 35–89.

50 C. Hampel, K. A. Peterson and H.-J. Werner, *Chem. Phys. Lett.*, 1992, **190**, 1–12.

51 M. J. Deegan and P. J. Knowles, *Chem. Phys. Lett.*, 1994, **227**, 321–326.

52 T. B. Adler, G. Knizia and H.-J. Werner, *J. Chem. Phys.*, 2007, **127**, 221106.

53 G. Knizia, T. B. Adler and H.-J. Werner, *J. Chem. Phys.*, 2009, **130**, 054104.

54 C. Hättig, D. P. Tew and A. Köhn, *J. Chem. Phys.*, 2010, **132**, 231102.

55 D. Kats and F. R. Manby, *J. Chem. Phys.*, 2013, **139**, 021102.

56 D. Kats, *J. Chem. Phys.*, 2014, **141**, 061101.

57 D. Kats, D. Kreplin, H.-J. Werner and F. R. Manby, *J. Chem. Phys.*, 2015, **142**, 064111.

58 K. A. Peterson, T. B. Adler and H.-J. Werner, *J. Chem. Phys.*, 2008, **128**, 84102.

59 K. E. Yousaf and K. A. Peterson, *J. Chem. Phys.*, 2008, **129**, 184108.

60 S. Kritikou and J. G. Hill, *J. Chem. Theory Comput.*, 2015, **11**, 5269–5276.

9502 | *Phys. Chem. Chem. Phys.*, 2025, **27**, 9491–9503

This journal is © the Owner Societies 2025

61 H. Hartwig and H. Dreizler, *Z. Naturforsch.*, 1996, **51a**, 923–932.

62 J. K. G. Watson, *Vibrational spectra and structure*, Elsevier Scientific Publishing Company, Amsterdam, 1977, vol. 6, pp. 1–89.

63 S. Herbers, P. Kraus and J.-U. Grabow, *J. Chem. Phys.*, 2019, **150**, 144308.

64 K. G. Lengsfeld, *PhD thesis*, Wilhelm Leibniz University Hannover, 2021.

65 J. Kraitchman, *Am. J. Phys.*, 1953, **21**, 17–24.

66 J. Demaison and H. Rudolph, *J. Mol. Spectrosc.*, 2002, **215**, 78–84.

67 H. Rudolph and J. Demaison, *Equilibrium Molecular Structures: From Spectroscopy to Quantum Chemistry*, 2011, pp. 125–158.

68 J. Demaison, J. E. Boggs and A. G. Császár, *Equilibrium molecular structures: from spectroscopy to quantum chemistry*, CRC Press, 2016.

69 Z. Kisiel, *J. Mol. Spectrosc.*, 2003, **218**, 58–67.

70 Z. Kisiel, *Spectroscopy from Space*, Springer, Netherlands, 2001, pp. 91–106.

71 H. M. Pickett, *J. Mol. Spectrosc.*, 1991, **148**, 371–377.

72 J. K. Watson, A. Roytburg and W. Ulrich, *J. Mol. Spectrosc.*, 1999, **196**, 102–119.

73 N. Vogt, E. P. Altova and N. M. Karasev, *J. Mol. Struct.*, 2010, **978**, 153–157.

74 M. K. Jahn, D. A. Obenchain, K. P. R. Nair, J.-U. Grabow, N. Vogt, J. Demaison, P. D. Godfrey and D. McNaughton, *Phys. Chem. Chem. Phys.*, 2020, **22**, 5170–5177.

75 N. O. Lüttschwager and M. A. Suhm, *Soft Matter*, 2014, **10**, 4885–4901.

76 T. Forsting, H. C. Gottschalk, B. Hartwig, M. Mons and M. A. Suhm, *Phys. Chem. Chem. Phys.*, 2017, **19**, 10727–10737.

77 M. Gawrilow and M. A. Suhm, *Molecules*, 2021, **26**, 4523.

78 M. C. Galanti and A. V. Galanti, *J. Org. Chem.*, 1982, **47**, 1572–1574.

79 A. Kanzow, B. Hartwig and D. A. Obenchain, Experimental XIAM and Kraitchman structure and semi-experimental as well as mass dependent structure fits for citraconic and itaconic anhydride, *GRO.data, V1*, 2025, DOI: **10.25625/AFCLSC**.

80 A. Kanzow, B. Hartwig and D. A. Obenchain, Computational outputs of DFT, MP2 and Coupled Cluster calculations for geometry optimizations and frequency calculations, *GRO.data, V1*, 2025, DOI: **10.25625/IBKABW**.

81 A. Kanzow, B. Hartwig, D. A. Obenchain and J.-U. Grabow, Microwave spectra of Citraconic and Itaconic anhydride, *GRO.data, V1*, 2025, DOI: **10.25625/FQCEVB**.

This journal is © the Owner Societies 2025

Phys. Chem. Chem. Phys., 2025, **27**, 9491–9503 | **9503**